We are IntechOpen, the world's leading publisher of Open Access books Built by scientists, for scientists

4,800
Open access books available

122,000
International authors and editors

135M
Downloads

154
Countries delivered to

Our authors are among the
TOP 1%
most cited scientists

12.2%
Contributors from top 500 universities

WEB OF SCIENCE™

Selection of our books indexed in the Book Citation Index
in Web of Science™ Core Collection (BKCI)

Interested in publishing with us?
Contact book.department@intechopen.com

3-D Finite-Element Modelling of a Maglev System using Bulk High-Tc Superconductor and its Application

Guang-Tong Ma[1,2], Jia-Su Wang[1] and Su-Yu Wang[1]
[1]Applied Superconductivity Laboratory of Southwest Jiaotong University,
[2]Traction Power State Key Laboratory of Southwest Jiaotong University,
P. R. China

1. Introduction

Maglev using bulk High-Tc superconductor can realize stable levitation without any active control (Brandt, 1989), and this facsinating property can reduce remarkably the complexity of the levitation system and therefore exhibits promising application in several fields such as maglev bearing (Hull, 2000; Ma, et al., 2003) and maglev transit (Wang, et al., 2002 ; Wang, J. & Wang, S., 2005; Schultz, et al., 2005; Sotelo, et al., 2010). To understand the electromagnetic interaction between the bulk high-Tc superconductor and its applied fields generated by various permanent magnetic devices and to provide a numerical tool to conduct the design for practical application, many methods have been proposed to numerically estimate the characteristics of the magnetic force of the bulk high-Tc superconductor.

The earliest method (Davis, et al., 1988) after the discovery of the high-Tc superconductor was basically established on the traditional mirror-image-model which uses Bean's critical model (Bean, 1964). However, this model and the later frozen-image model (Kordyuk, 1998) can not reflect the important hysteresis property of the levitation force (Hull & Cansiz, 1999). Though this demerit can be overcome to some extent by introducing additional image dipoles (Yang & Zheng, 2007), this kind of model is essentially a phenomenological one and its applicable scope is also confined to miniature scale systems due to the essential dipole approximation of the levitated body in deducing the model.

Based on the principle of minimum energy, the current distribution in the high-Tc superconductor can be acquired by an iterative process, and then the magnetic force of the high-Tc superconductor can be calculated by Lorentz equation (Sanchez & Navau, 2001; Navau & Sanchez, 2001; Sanchez, et al., 2006). However, up to date, this method is used only to investigate the axisymmetric system with cylindrical high-Tc superconductor and permanent magnet (Navau & Sanchez, 2001) or 2-D translational symmetry system with rectangular high-Tc superconductor and permanent magnetic array (Sanchez, et al., 2006).

According to the state variables used in the governing equations, the methods describing the electromagnetic property of the high-Tc superconductor based on Maxwell's equations can be classified into three types, i.e., **A**-*V*-method (Prigozhin, 1997), *T*-method (Hashizume, et al., 1991), and *H*-method (Pecher, et al., 2003). Most previous work (Qin, et al., 2002; Uesaka, et al., 1993; Yoshida, et al., 1994; Luo, et al., 1999; Alonso, et al., 2004;

Gou, et al.,2007a; Gou, et al.,2007b) using these methods was to calculate the levitation force of a bulk high-Tc superconductor by aid of the assumption that the induced current only flows in the *ab*-plane of the high-Tc superconductor. In this case, only the component of the state variable along the *c*-axis of the high-Tc superconductor is considered in the governing equation and the number of degrees of freedom is therefore reduced and the problem to be solved is actually a 2-D one. This assumption is acceptable when the studied problem has an axisymmetric geometry and the movement of the bulk high-Tc superconductor is restricted to the vertical direction above the center of the magnetic device because in this situation, the induced current in the high-Tc superconductor due to the variation of the applied field will flow along the plane parallel to the *ab*-plane. As a result, the numerical results of the levitation force compare well with the measured data (Uesaka, et al., 1993; Alonso, et al., 2004; Gou, et al.,2007a), but for other situations, e.g., a bulk high-Tc superconductor is above a rectangular permanent magnet or a magnetic rail, the assumption is no longer satisfied and modelling high-Tc superconductor in full 3-D case is thereby required. Based on the **A**-*V*-method, the 3-D model has been proposed to numerically estimate the characteristics of the levitation force as well as the lateral force of a levitating transporter using bulk high-Tc superconductor (Ueda, et al., 2006), and also the dynamic behavior of the levitation system composed of a rectangular high-Tc superconductor and permanent magnet (Alloui, et al., 2009). However, though an anisotropic critical model is employed in the numerical iterative proces (Ueda, et al., 2006), none of them has considered the special electromagnetic anisotropic behavior of the high-Tc superconductor in deducing the governing equations. Those models are hence still an anisotropic 3-D model. For the maglev transit using bulk high-Tc superconductor above a magnetic rail, a 3-D model considering the anisotropic behavior is reported (Lu, et al., 2008). In their model, in order to describe the anisotropic behavior, the bulk high-Tc superconductor is split into two different parts: One is a homogeneous part that is identical to an anisotropic superconductor, and the other is considered as a conductor whose conductivity only along the *c*-axis is not equal to zero. However, the reasonable explanation of this superposition approach to describe the anisotropic behavior in physics is still a question needed to be answered at present.

In this chapter, we report a 3-D finite-element model using current potential **T** as state variable. In this model, the anisotropic behavior of the high-Tc superconductor is contained in the 3-D governing equations by considering a tensor resistivity, and the finite-element technique is empolyed to numerically solve the mathmatical formulations on a VC++ software platform. The numerical results of both levitation force and lateral force were validated by the measured data. Lastly, one example using this 3-D finite-element model to optimize the magnetic rail is introduced to present its viable use for practical design of maglev system using bulk high-Tc superconductor.

2. Mathematical formulations

2.1 Formulations to model the anisotropy in high-Tc superconductor

The special microstructure, which consists of the alternating stack of superconductive CuO_2 layers and almost insulating block layers, results in a remarkable anisotropic behavior in the present high-Tc superconductor (Dinger, et al., 1987). Due to this anisotropic behavior arising from the intrinsic pinning and other defects in the high-Tc superconductor, the flux-line curvature will always occur when the high-Tc superconductor is placed in a magnetic field.
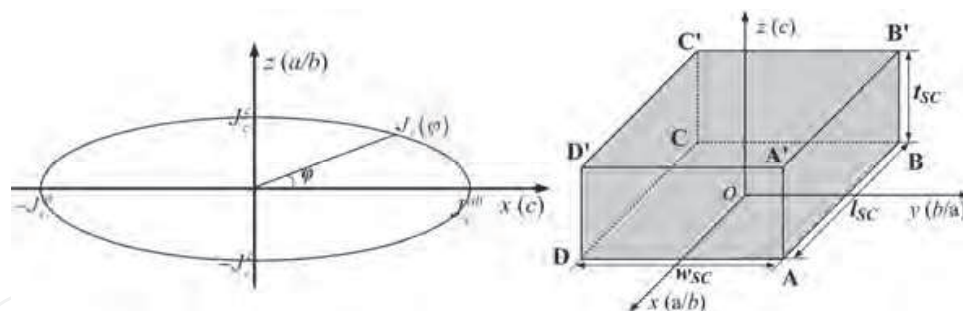
Fig. 1. Schematic drawing of the elliptical model (left) and the Cartesian coordinate system with a bulk high-Tc superconductor whose *c*-axis is parallel to the *z*-axis (right).

Consequently, the critical current density J_c of the high-Tc superconductor is anisotropic and strongly dependent on the orientation of the applied field (Mikitik & Brandt, 2000). Namely, the value of the critical current density flowing in the *ab*-plane J_c^{ab} is larger than that along the *c*-axis J_c^c (Matsushita, 2007).

Many methods have been proposed to formulate the dependence of the critical current density J_c on the angle φ between the orientation of the local applied field and *c*-axis. However, a few of them are difficult to be employed in the present calculation due to its complexity in determining the parameters involved in the formulation (Mikitik & Brandt, 2000) or its applicable field range is beyond our focus (Sawamura & Tsuchimoto, 2000). Another model reported in (Yang, et al., 1999) is simple to be employed and has been valiadated in an axisymmetric levitation system. This model is desribed in the following:

When the out-of-plane anisotropic ratio *a* of the critical current density J_c is defined as $a = J_c^{ab}/J_c^c$, the $J_c(\varphi)$ relation can be rewritten as follows:

$$J_c\left(\varphi\right) = J_c^{ab}\left(\cos^2\varphi + \sin^2\varphi/\alpha\right) \tag{1}$$

Here, we will introduce an elliptical model, which has been used to investigate the electromagnetic problem involving the anisotropic ferromagnetic material (Napoli & Paggi, 1983), to describe the angular-dependence property of the critical current density J_c in the high-Tc superconductor. According to the schematic drawing shown in Fig. 1, the elliptic model can be expressed by the following equation:

$$\left(\frac{J_{cx}}{J_c^{ab}}\right)^2 + \left(\frac{J_{cz}}{J_c^c}\right)^2 = 1 \tag{2}$$

where J_{cx} and J_{cz} are the induced current densities in the *ab*-plane and parallel to the *c*-axis, respectively. According to (2), the $J_c(\varphi)$ relation with respect to J_c^{ab} and *a* can be expressed as:

$$J_c\left(\varphi\right) = \sqrt{J_{cx}^2 + J_{cz}^2} = J_c^{ab}\sqrt{\cos^2\varphi + \left(\sin\varphi/\alpha\right)^2} \tag{3}$$

The resistivity of the high-Tc superconductor is also anisotropic (Wu, et al., 1991) and can be represented by a tensor while modelling the high-Tc superconductor. The tensor of the resistivity of the high-Tc superconductor can be reduced to a following diagonal matrix when only the out-of-plane anisotropy is considered,

$$\overline{\overline{\rho_s}} = \begin{bmatrix} \rho_{ab} & 0 & 0 \\ 0 & \rho_{ab} & 0 \\ 0 & 0 & \rho_c \end{bmatrix} = \begin{bmatrix} \rho_{ab} & 0 & 0 \\ 0 & \rho_{ab} & 0 \\ 0 & 0 & \alpha\rho_{ab} \end{bmatrix}$$

where ρ_{ab} and ρ_c are the resistivity in the *ab*-plane and along the *c*-axis, respectively. It is important to remark here that, for the identical electrical field criterion E_c to determine the critical current density J_c, the anisotropic ratio of the resistivity ρ and the critical current density J_c are reciprocal to each other. The above tensor expression of the resistivity illustrates a possible way to establish the governing equations of the high-Tc superconductor including its anisotropic behavior.

2.2 3-D governing equations

The *T*-method is adopted in our model because it has the merits that, the number of unknown and space needed to be meshed can be remarkably reduced because the variable *T* can be defined as zero outside the conductor (Miya & Hashizume, 1988).
As a conducting material, Maxwell's equations are also valid to describe the electromagnetic phenomena in the high-Tc superconductor. Thus, we have,

$$\nabla \times \mathbf{H} = \mathbf{J} \tag{4}$$

$$\nabla \times \mathbf{E} = -\frac{\partial \mathbf{B}}{\partial t} \tag{5}$$

According to (4), the current density $\mathbf{J}$ is a divergence free vector with a quasi-static approximation in the low-frequency problem, i.e., $\nabla \cdot \mathbf{J} = 0$, and thus, a current vector potential $\mathbf{T}$ can be introduced and defined as,

$$\mathbf{J} = \nabla \times \mathbf{T} \tag{6}$$

The Coulomb gauge is applied to vector $\mathbf{T}$ to guarantee the uniqueness of the solution, i.e., $\nabla \cdot \mathbf{T} = 0$. Applying Helmholtz's theorem to vector $\mathbf{T}$ yields the following equation:

$$C(P)\mathbf{T}(P) = \frac{1}{4\pi}\int_V \left(\nabla' \cdot \mathbf{T}(P')\right)\nabla' \frac{1}{R(P,P')}dV' - \frac{1}{4\pi}\int_S \left(\mathbf{n}' \cdot \mathbf{T}(P')\right)\nabla' \frac{1}{R(P,P')}dS'$$
$$+ \frac{1}{4\pi}\int_V \left(\nabla' \times \mathbf{T}(P')\right) \times \nabla' \frac{1}{R(P,P')}dV' - \frac{1}{4\pi}\int_S \left(\mathbf{n}' \times \mathbf{T}(P')\right) \times \nabla' \frac{1}{R(P,P')}dS' \tag{7}$$

where $R(P, P')$ is the distance between the source point P' and the field point P, the superscript ' refers to the quantity at the source point, $\mathbf{n}'$ is a unit vector out of the surface S', and the coefficient $C(P)$ takes the following values (Hashizume, et al., 1991)：

$$C(P) = \begin{cases} 1 & P \in V' \ (excluding \ S') \\ 1/2 & P \in S' \\ 0 & elsewhere \end{cases}$$

According to the physical fact that the normal component of $\mathbf{J}$ must be zero on the surface of the high-Tc superconductor, i.e., $J_n = 0$, $\mathbf{T}$ has the following boundary condition (Miya & Hashizume, 1988):

$$\mathbf{n}' \times \mathbf{T} = 0 \tag{8}$$

Therefore, only the normal component T_n exists on all the surfaces of the high-Tc superconductor, e.g., for the surface of AA'D'D as shown in Fig.1, vector $\mathbf{T}$ is reduced to a scalar T_x. Furthermore, T is zero on all edges of the rectangular high-Tc superconductor bulk, e.g., for edge AA' as shown in Fig.1, when it is regarded as a part of surface AA'D'D, $T_y = T_z = 0$, whereas when it is considered as a part of surface AA'B'B, $T_x = T_z = 0$. Thus, we have $T_x = T_y = T_z = 0$ on all the edges.

Equation (7) is reduced to the following form when the Coulomb gauge and boundary condition (8) are considered,

$$C(P)\mathbf{T}(P) = \frac{1}{4\pi}\int_V \left(\nabla' \times \mathbf{T}(P')\right) \times \nabla' \frac{1}{R(P,P')} dV' - \frac{1}{4\pi}\int_S \left(\mathbf{n}' \cdot \mathbf{T}(P')\right)\nabla' \frac{1}{R(P,P')} dS' \tag{9}$$

The *B-H* constitutive law of the high-Tc superconductor can be assumed to be linear as that in vacuum with a good approximation because its applicable conditions (Brandt, 1996) can be easily satisfied in a levitation system using bulk Y-Ba-Cu-O due to its small lower critical field B_{c1} (Krusin-Elbaum, et al., 1989) and large applied field as well as geometry. Thus,

$$\mathbf{B} = \mu_0 \mathbf{H} \tag{10}$$

The induced field $\mathbf{B}_s$ produced by the induced current in the high-Tc superconductor can be expressed in terms of the vector $\mathbf{T}$ in the following equation when we combine (9) with Biot-Savart's law (Miya & Hashizume, 1988),

$$\mathbf{B}_s = \mu_0 C(P)\mathbf{T}(P) + \frac{\mu_0}{4\pi}\int_S \left(\mathbf{n}' \cdot \mathbf{T}(P')\right)\nabla' \frac{1}{R(P,P')} dS' \tag{11}$$

When an equivalent conductivity σ_s, which is nonlinear and dependent on the local electrical field of the high-Tc superconductor, is introduced, the traditional Ohm's law in the high-Tc superconductor has the following form:

$$\mathbf{J} = \sigma_s\left(|\mathbf{E}|\right)\mathbf{E} \tag{12}$$

By substituting (6) and (12) into (5) and considering $\mathbf{B} = \mathbf{B}_e + \mathbf{B}_s$ where $\mathbf{B}_e$ is the applied field, yields the following equation:

$$\nabla \times \frac{1}{\sigma_s}(\nabla \times \mathbf{T}) + \frac{\partial(\mathbf{B}_e + \mathbf{B}_s)}{\partial t} = 0 \tag{13}$$

The governing equation of the high-Tc superconductor based on the variable *T* is finally derived from (11), and (13) as follows,

$$\nabla \times \frac{1}{\sigma_s}(\nabla \times \mathbf{T}) + \mu_0 C(P)\frac{\partial \mathbf{T}}{\partial t} + \frac{\mu_0}{4\pi}\int_S \frac{\partial(\mathbf{n}' \cdot \mathbf{T}')}{\partial t}\nabla' \frac{1}{R(P,P')} dS' + \frac{\partial \mathbf{B}_e}{\partial t} = 0 \tag{14}$$

When we replace σ_s by a tensor resistivity $\overline{\overline{\rho_s}}$, (14) and consider that,

$$\overline{\overline{\rho_s}}(\nabla \times \mathbf{T}) = \begin{bmatrix} \rho_{ab} & 0 & 0 \\ 0 & \rho_{ab} & 0 \\ 0 & 0 & \alpha\rho_{ab} \end{bmatrix} \begin{bmatrix} \left(\dfrac{\partial T_z}{\partial y} - \dfrac{\partial T_y}{\partial z}\right)\hat{\boldsymbol{x}} \\ \left(\dfrac{\partial T_x}{\partial z} - \dfrac{\partial T_z}{\partial x}\right)\hat{\boldsymbol{y}} \\ \left(\dfrac{\partial T_y}{\partial x} - \dfrac{\partial T_x}{\partial y}\right)\hat{\boldsymbol{z}} \end{bmatrix} = \rho_{ab}\left[\left(\dfrac{\partial T_z}{\partial y} - \dfrac{\partial T_y}{\partial z}\right)\hat{\boldsymbol{x}} + \left(\dfrac{\partial T_x}{\partial z} - \dfrac{\partial T_z}{\partial x}\right)\hat{\boldsymbol{y}} + \alpha\left(\dfrac{\partial T_y}{\partial x} - \dfrac{\partial T_x}{\partial y}\right)\hat{\boldsymbol{z}}\right] \tag{15}$$

The following equality for the first term in the left side of (14) is satisfied,

$$\nabla \times \frac{1}{\sigma_s}(\nabla \times \mathbf{T}) = \nabla \times \overline{\overline{\rho_s}}(\nabla \times \mathbf{T}) = \rho_{ab}\left[\alpha\frac{\partial^2 T_y}{\partial x \partial y} - \alpha\frac{\partial^2 T_x}{\partial y^2} - \frac{\partial^2 T_x}{\partial z^2} + \frac{\partial^2 T_z}{\partial x \partial z}\right]\hat{\boldsymbol{x}}$$
$$+ \rho_{ab}\left[\frac{\partial^2 T_z}{\partial y \partial z} - \frac{\partial^2 T_y}{\partial z^2} - \alpha\frac{\partial^2 T_y}{\partial x^2} + \alpha\frac{\partial^2 T_x}{\partial y \partial x}\right]\hat{\boldsymbol{y}} + \rho_{ab}\left[\frac{\partial^2 T_x}{\partial z \partial x} - \frac{\partial^2 T_z}{\partial x^2} - \frac{\partial^2 T_z}{\partial y^2} + \frac{\partial^2 T_y}{\partial z \partial y}\right]\hat{\boldsymbol{z}} \tag{16}$$

According to the Coulomb gauge, we have $\nabla(\nabla \cdot \mathbf{T}) = 0$ i.e.,

$$\left(\frac{\partial^2 T_x}{\partial x^2} + \frac{\partial^2 T_y}{\partial y \partial x} + \frac{\partial^2 T_z}{\partial z \partial x}\right)\hat{\boldsymbol{x}} + \left(\frac{\partial^2 T_x}{\partial x \partial y} + \frac{\partial^2 T_y}{\partial y^2} + \frac{\partial^2 T_z}{\partial z \partial y}\right)\hat{\boldsymbol{y}} + \left(\frac{\partial^2 T_x}{\partial x \partial z} + \frac{\partial^2 T_y}{\partial y \partial z} + \frac{\partial^2 T_z}{\partial z^2}\right)\hat{\boldsymbol{z}} = 0 \tag{17}$$

The following identities can be derived from (17),

$$\frac{\partial^2 T_z}{\partial z \partial x} = -\frac{\partial^2 T_x}{\partial x^2} - \frac{\partial^2 T_y}{\partial y \partial x}, \qquad \frac{\partial^2 T_z}{\partial z \partial y} = -\frac{\partial^2 T_x}{\partial x \partial y} - \frac{\partial^2 T_y}{\partial y^2}, \qquad \frac{\partial^2 T_x}{\partial x \partial z} + \frac{\partial^2 T_y}{\partial y \partial z} = -\frac{\partial^2 T_z}{\partial z^2} \tag{18}$$

Equality (16) can be further written in the following way when (18) is taken into account,

$$\nabla \times \overline{\overline{\rho_s}}(\nabla \times \mathbf{T}) = \rho_{ab}\left[-\frac{\partial^2 T_x}{\partial x^2} - \alpha\frac{\partial^2 T_x}{\partial y^2} - \frac{\partial^2 T_x}{\partial z^2} + (\alpha - 1)\frac{\partial^2 T_y}{\partial x \partial y}\right]\hat{\boldsymbol{x}}$$
$$+ \rho_{ab}\left[-\alpha\frac{\partial^2 T_y}{\partial x^2} - \frac{\partial^2 T_y}{\partial y^2} - \frac{\partial^2 T_y}{\partial z^2} + (\alpha - 1)\frac{\partial^2 T_x}{\partial x \partial y}\right]\hat{\boldsymbol{y}} + \rho_{ab}\left(-\frac{\partial^2 T_z}{\partial x^2} - \frac{\partial^2 T_z}{\partial y^2} - \frac{\partial^2 T_z}{\partial z^2}\right)\hat{\boldsymbol{z}}. \tag{19}$$

Besides,

$$\nabla'\frac{1}{R(P,P')} = \frac{\partial}{\partial x'}\left(\frac{1}{R(P,P')}\right)\hat{\boldsymbol{x}} + \frac{\partial}{\partial y'}\left(\frac{1}{R(P,P')}\right)\hat{\boldsymbol{y}} + \frac{\partial}{\partial z'}\left(\frac{1}{R(P,P')}\right)\hat{\boldsymbol{z}}, \tag{20}$$

and

$$\mathbf{B}_e = B_{ex}\hat{\boldsymbol{x}} + B_{ey}\hat{\boldsymbol{y}} + B_{ez}\hat{\boldsymbol{z}}. \tag{21}$$

Finally, the following 3-D governing equations are obtained once (19) to (21) are substituted into (14) and ρ_{ab} is replaced by its reciprocal σ_{ab}.

$$\frac{1}{\sigma_{ab}}\left(-\frac{\partial^2 T_x}{\partial x^2}-\alpha\frac{\partial^2 T_x}{\partial y^2}-\frac{\partial^2 T_x}{\partial z^2}+(\alpha-1)\frac{\partial^2 T_y}{\partial x\partial y}\right)+\mu_0 C(P)\frac{\partial T_x}{\partial t}+\frac{\mu_0}{4\pi}\int_S\frac{\partial(\mathbf{n'\cdot T'})}{\partial t}\frac{\partial}{\partial x'}\left(\frac{1}{R(P,P')}\right)dS'+\frac{\partial B_{ex}}{\partial t}=0 \tag{22}$$

$$\frac{1}{\sigma_{ab}}\left(-\alpha\frac{\partial^2 T_y}{\partial x^2}-\frac{\partial^2 T_y}{\partial y^2}-\frac{\partial^2 T_y}{\partial z^2}+(\alpha-1)\frac{\partial^2 T_x}{\partial x\partial y}\right)+\mu_0 C(P)\frac{\partial T_y}{\partial t}+\frac{\mu_0}{4\pi}\int_S\frac{\partial(\mathbf{n'\cdot T'})}{\partial t}\frac{\partial}{\partial y'}\left(\frac{1}{R(P,P')}\right)dS'+\frac{\partial B_{ey}}{\partial t}=0 \tag{23}$$

$$\frac{1}{\sigma_{ab}}\left(-\frac{\partial^2 T_z}{\partial x^2}-\frac{\partial^2 T_z}{\partial y^2}-\frac{\partial^2 T_z}{\partial z^2}\right)+\mu_0 C(P)\frac{\partial T_z}{\partial t}+\frac{\mu_0}{4\pi}\int_S\frac{\partial(\mathbf{n'\cdot T'})}{\partial t}\frac{\partial}{\partial z'}\left(\frac{1}{R(P,P')}\right)dS'+\frac{\partial B_{ez}}{\partial t}=0 \tag{24}$$

where σ_{ab} is the conductivity in the *ab*-plane. It is worth noting that, compared with the traditional T-Ω method, the complexity of the governing equations is reduced due to the omission of the variable Ω (Miya & Hashizume, 1988), and thus the number of varibles in the problem is three with unknown T_x, T_y, and T_z.

2.3 Nonlinear E-J relations

Typically, there are three different models to address the highly nonlinear relationship between **E** and **J** of the high-Tc superconductor, i.e., Bean's critical current model (Bean, 1964), power law model (Rhyner, 1993) and flux flow and creep model (Yamafuji & Mawatari, 1992). For Bean's critical current model, it fails to investigate problems such as force relaxation (Luo, et al., 1999) and drift under vibration (Gou, et al., 2007) due to the assumption that the current flowing in the superconductor is constant with time and the lack of material related parameters in its model. In addition, Bean's critical current model can be considered as an infinite case of the power law model (Rhyner, 1993). This model is thereby not employed in the following calculation.

When an index n is introduced and defined as $n=U_0/k\Theta$ where U_0 is the pinning potential of the superconductor at an absolute temperature Θ and k is the Boltzmann constant, the power law model is expressed as:

$$\mathbf{E}=E_c\left(|\mathbf{J}|/J_c\right)^n \mathbf{J}/|\mathbf{J}| \tag{25}$$

According to Anderson theory (Anderson, 1962), the responding behavior between **E** and **J** due to flux flow and creep model phenomena in the superconductor can be described as:

$$\mathbf{E}=\begin{cases}2\rho_c J_c\sinh(\frac{U_0}{\kappa\Theta}\frac{|\mathbf{J}|}{J_c})\exp(-\frac{U_0}{\kappa\Theta})\frac{\mathbf{J}}{|\mathbf{J}|} & 0\le|\mathbf{J}|\le J_c \\ E_c+\rho_f J_c(\frac{|\mathbf{J}|}{J_c}-1)\frac{\mathbf{J}}{|\mathbf{J}|} & |\mathbf{J}|>J_c\end{cases} \tag{26}$$

where ρ_c and ρ_f are the creep and flow resistivities respectively, and $E_c=\rho_c J_c\left[1-\exp(-2U_0/\kappa\Theta)\right]\approx\rho_c J_c$.

3. Numerical solution using finite-element technique

The previous work in handling linear eddy current problem has proven that Boundary Element Method is an effective method to numerically solve the governing equations including both differential and integral terms (Miya & Hashizume, 1988). Unfortunately, for the case studied here, the high-Tc superconductor is a highly nonlinear media, and this special property leads to difficulty when Boundary Element Method is employed to handle the 3-D governing equations. Consequently, the finite element method is a frequent choice to discretize the governing equation of the high-Tc superconductor in space (Pecher, et al., 2003; Uesaka, et al., 1993; Yoshida, et al., 1994; Luo, et al., 1999; Alonso, et al., 2004; Gou, et al.,2007a; Gou, et al.,2007b; Lu, et al., 2008). In particular, one format of the finite difference method, named Crank-Nicolson-θ method, is employed to numerically perform the time domain of the 3-D governing equations.

3.1 Finite-element matrices
The governing equations (22) to (24) incorporated with the boundary condition are numerically solved by finite-element technique via Galerkin's method. The tetrahedral element is chosen to mesh the domain of the high-Tc superconductor. The final algebraic equations corresponding to (22) to (24) can be compactly expressed by the following matrix equation,

$$\left[\mathbf{K}_i\left(\sigma_{ab}\right)\right]\{T_i\}+\left[\mathbf{K}_{12}\left(\sigma_{ab}\right)\right]\{T_{3-i}\}+\left[\mathbf{Q}_{0i}\right]\left\{\frac{\partial T_i}{\partial t}\right\}+\left[\mathbf{Q}_{1i}\right]\left\{\frac{\partial(\mathbf{n'\cdot T'})}{\partial t}\right\}=\{\mathbf{L}_i\}\ (i=1,2,3) \tag{27}$$

where

$$\left[\mathbf{K}_i\left(\sigma_{ab}\right)\right]=\sum_e\left[\mathbf{K}_i\left(\sigma_{ab}^e\right)\right]_e=\sum_e\frac{1}{\sigma_{ab}^e}\int_{V_e}\left(\alpha_i\left[\frac{\partial N}{\partial x}\right]_e^{\mathrm{T}}\left[\frac{\partial N}{\partial x}\right]_e+\alpha_{3-i}\left[\frac{\partial N}{\partial y}\right]_e^{\mathrm{T}}\left[\frac{\partial N}{\partial y}\right]_e+\left[\frac{\partial N}{\partial z}\right]_e^{\mathrm{T}}\left[\frac{\partial N}{\partial z}\right]_e\right)dV$$

$$\left[\mathbf{K}_{12}\left(\sigma_{ab}\right)\right]=\sum_e\left[\mathbf{K}_{12}\left(\sigma_{ab}^e\right)\right]_e=\frac{1}{2}(1-\alpha)\sum_e\frac{1}{\sigma_{ab}^e}\int_{V_e}\left(\frac{\partial[N]_e^{\mathrm{T}}}{\partial y}\frac{\partial[N]_e}{\partial x}+\frac{\partial[N]_e^{\mathrm{T}}}{\partial x}\frac{\partial[N]_e}{\partial y}\right)dV$$

i	K_i	T_i	T_{3-i}	Q_{0i}	Q_{1i}	L_i	α_i	α_{3-i}	u'_i	B_{ei}
1	K_x	T_x	T_y	Q_{0x}	Q_{1x}	L_x	1	α	x'	B_{ex}
2	K_y	T_y	T_x	Q_{0y}	Q_{1y}	L_y	α	1	y'	B_{ey}
3	K_z	T_z	0	Q_{0z}	Q_{1z}	L_z	1	1	z'	B_{ez}

Table 1. Specification of the variable parameters in (27)

$$[\mathbf{Q}_{0i}]=\sum_e[\mathbf{Q}_{0i}]_e=\mu_0\sum_e\int_{V_e}[N]_e^{\mathrm{T}}\left[C(P)N\right]_e dV$$

$$[\mathbf{Q}_{1i}]=\sum_e[\mathbf{Q}_{1i}]_e=\frac{\mu_0}{4\pi}\sum_e\int_{V_e}[N]_e^{\mathrm{T}}\left(\int_S[N]_e\frac{\partial}{\partial u'_i}\frac{1}{R(P,P')}dS'\right)dV$$

$$\{\mathbf{L}_i\}=\sum_e\{\mathbf{L}_i\}_e=-\sum_e\int_{V_e}[N]_e^{\mathrm{T}}\frac{\partial B_{ei}}{\partial t}dV$$

3-D Finite-Element Modelling of a Maglev System
using Bulk High-Tc Superconductor and its Application
127

N is the shape function of the linear tetrahedral nodal element. The subscript e represents its detailed formula in each element. The conductivity is different for each element and it is therefore represented by σ_{ab}^e here. All the other parameters with a subscript including i can be determined by Table 1.

The finite-element matrices (27) for three components are integrated into one matrix in the numerical program, i.e.,

$$\left[\mathbf{K}(\sigma_{ab})\right]\{T\}+\left[\mathbf{Q}_0\right]\left\{\frac{\partial T}{\partial t}\right\}+\left[\mathbf{Q}_1\right]\left\{\frac{\partial(\mathbf{n'}\cdot\mathbf{T'})}{\partial t}\right\}=\{\mathbf{L}\} \tag{28}$$

where

$$\left[\mathbf{K}(\sigma_{ab})\right]=\sum_{i=1}^{2}\left[\left[\mathbf{K}_i(\sigma_{ab})\right]+\left[\mathbf{K}_{12}(\sigma_{ab})\right]\right]+\left[\mathbf{K}_3(\sigma_{ab})\right]$$

$$\left[\mathbf{Q}_0\right]=\sum_{i=1}^{3}\left[\mathbf{Q}_{0i}\right] \qquad \left[\mathbf{Q}_1\right]=\sum_{i=1}^{3}\left[\mathbf{Q}_{1i}\right] \qquad \{\mathbf{L}\}=\sum_{i=1}^{3}\{\mathbf{L}_i\}$$

After applying Crank-Nicolson-θ method to (28) for time discretization, the matrix at nth time step can be written as:

$$\left(\frac{[\mathbf{Q}_0]+[\mathbf{Q}_1]}{\Delta t}+\theta\left[\mathbf{K}(\sigma_{ab})\right]\right)\{T^n\}=\theta\{\mathbf{L}^n\}+(1-\theta)\{\mathbf{L}^{n-1}\}+\left(\frac{[\mathbf{Q}_0]+[\mathbf{Q}_1]}{\Delta t}-(1-\theta)\left[\mathbf{K}(\sigma_{ab})\right]\right)\{T^{n-1}\} \tag{29}$$

The disadvantage of the T-method is that the coefficient of (29) is a dense matrix. In the previous work, an over-relaxation iterative solution approach has been proposed to handle this dense matrix on a linear eddy current problem (Takagi, et al., 1988). However, to the situation we are facing, the nonlinearity of the E–J characteristic brings an additional iterative procedure in determining the conductivity of the high-Tc superconductor. Therefore, if the over-relaxation approach is employed in our computation, there would be two iterative procedures in the numerical program, and this would give rise to numerical instability in the calculation as well as the complexity of the numerical program. The dense feature of the coefficient matrix of (29) arises from the dense matrix $[Q_1]$, which is related to the integral term of (27). Therefore, the coefficient matrix will be a sparse one if $[Q_1]$ is transferred to the right side of (29), and this operation gives the following form,

$$\left(\frac{[\mathbf{Q}_0]}{\Delta t}+\theta\left[\mathbf{K}(\sigma_{ab})\right]\right)\{T^n\}=\theta\{\mathbf{L}^n\}+(1-\theta)\{\mathbf{L}^{n-1}\}+\left(\frac{[\mathbf{Q}_0]}{\Delta t}-(1-\theta)\left[\mathbf{K}(\sigma_{ab})\right]\right)\{T^{n-1}\}-[\mathbf{Q}_1]\{T^{n-1}-T^{n-2}\} \tag{30}$$

In (30), the dense matrix $[Q_1]$ is related to the difference of unknown variables between the last and the previous two time steps. The value of the unknown at the adjacent time step will approach to each other as the continuous decrease of the time step size $\triangle t$. Therefore, in order to obtain a higher precision, we should assign a sufficient small time step size.

3.2 Nonlinear equation solution approach

The common Newton-Raphson method is employed to solve the nonlinear equations obtained from (30). Basically, the nonlinearity of the equations is eliminated by introducing a linear residual, and the corresponding linear equations can be integrated after calculating

the Jacobi matrix for each element. To improve the stability of the calculation, a relaxation coefficient is also introduced as suggested in (Grilli, et al., 2005). The relaxation coefficient is assigned with an initial value before calculation. During the calculation, it will be reduced to a smaller one once the convergence can not be achieved within a threshold of the total iterative steps, and in this case the current time step is recalculated with the new value.

Because of the significant increase of the order of the coefficient matrix when the problem is extended from 2-D to 3-D and also the element of the matrix with the anisotropy consideration involved (an additional second derivative in term of x and y appears in (22) and (23) when the anisotropic behavior is taken into account), the Incomplete Cholesky-Conjugate Gradient method (Kershaw, 1978), which is regarded as an effective approach to solve linear algebraic equations with large symmetric positive definite matrix, is employed to solve the linear equations at each iterative step in an accelerated form. In this accelerated form, an accelerated factor is introduced in the incomplete decomposition process (Fujiwara, et al., 1993) after the coefficient matrix and column vector are preconditioned by a method proposed in (Cui, 1989).

3.3 Numerical procedure

The above-discussed numerical method is implemented by a self-written numerical program based on a VC++ platform with the following typical steps:

Step 1: Initial σ_{ab} in all elements is assumed to be the same and sufficiently large value before the first time step.

Step 2: Calculating $[\mathbf{K}(\sigma_{ab})]$ with the present σ_{ab} in each element at the current time step, and vector $\mathbf{T}$ is obtained by solving (30).

Step 3: The σ_{ab} at the kth iterative step (σ_{ab}^k) is calculated in each element according to the following method using either power law model or flux flow and creep model.

If $J_c(\varphi)$ is expressed by (1),

$$\sigma_{ab}^k = |\mathbf{J}_k|/|\mathbf{E}_k|\Big/\left(\cos^2 \varphi + \sin^2 \varphi/\alpha\right) \tag{31}$$

If $J_c(\varphi)$ is expressed by (3),

$$\sigma_{ab}^k = |\mathbf{J}_k|/|\mathbf{E}_k|\Big/\sqrt{\cos^2 \varphi + \left(\sin \varphi/\alpha\right)^2} \tag{32}$$

At the end, σ_{ab} in each element is replaced by its new value σ_{ab}^k.

Step 4: Repeating steps 2 and 3 until the residual becomes less than a prescribed tolerance ε, i.e.,

$$\left[b - f\left(\mathbf{T}^{(k)}\right)\right]^2 < \varepsilon \tag{33}$$

where b is a column vector corresponding to the right side of (30), and $f(\mathbf{T}^{(k)})$ is the result of the left side of (30) at the kth iterative step.

Step 5: The current density $\mathbf{J}$ is obtained by (6), and then the magnetic force is calculated by Lorentz equation,

$$\mathbf{F} = \int_V \mathbf{J} \times \mathbf{B}_e dV \tag{34}$$

Step 6: $t = t + \Delta t$ until the maximum number of time step is achieved, and the steps 2-5 are repeated.

3.4 Numerical precision

Based on a levitation system composed of a bulk high-Tc superconductor（single-domain with a cubical shape）and magnetic rail（assembled by the permanent magnets with opposite magnetization direction as shown in the inset of Fig. 2）, the dependence of the computational precision of the levitation force on both mesh density and time step is discussed in this section. In the calculation, the bulk high-Tc superconductor was downward in a speed of 1 mm/s from the filed cooling position to the nearest gap, and then upward to its original position. On the basis of the geometrical and material parameters listed in Table 2 and power law model, the levitation force of the bulk high-Tc superconductor was calculated in this vertical down-and-up movement with different mesh densities and time steps.

w_{SC} (mm)	l_{SC} (mm)	t_{SC} (mm)	J_c^{ab} (A/m²)	E_c (V/m)	U_0 (EV)	a
10	10	10	$2.5×10^8$	$1×10^{-4}$	0.1	3

Table 2. Parameters of high-Tc superconductor used in the calculation for investigating the numerical precision.

Fig. 2 shows the dependence of the levitation force versus gap curve and the maximum levitation force F_{max} at the nearest gap on the total finite element node. This figure clearly illustrates that the levitation force and its hysteresis behavior will approach to a saturated state with the continuous increment of the total finite element node, or in other words, the continuous increment of the mesh density. It can be seen from the inset that the F_{max} continuously increases with the total finite element node but the increased rate is gradually
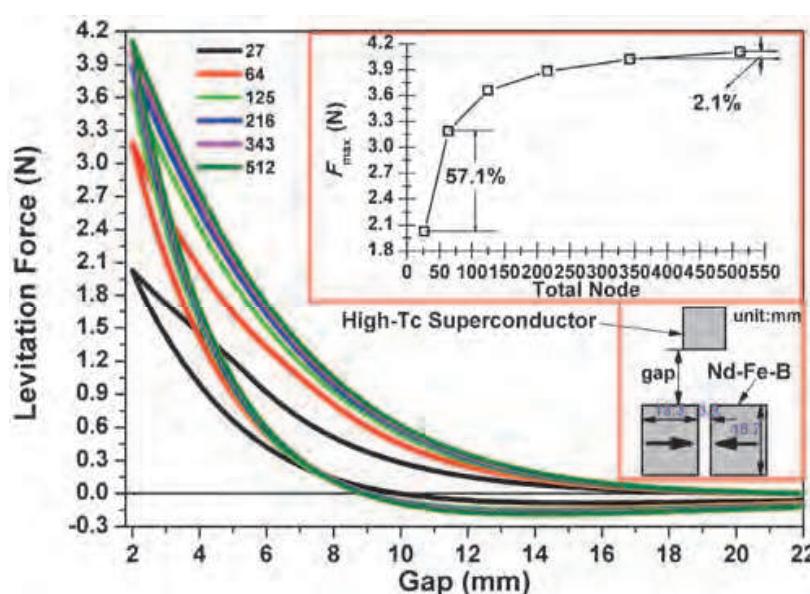
Fig. 2. Levitation force versus gap with different total nodes and the maximum levitation force F_{max} as a function of the total finite element node (inset).
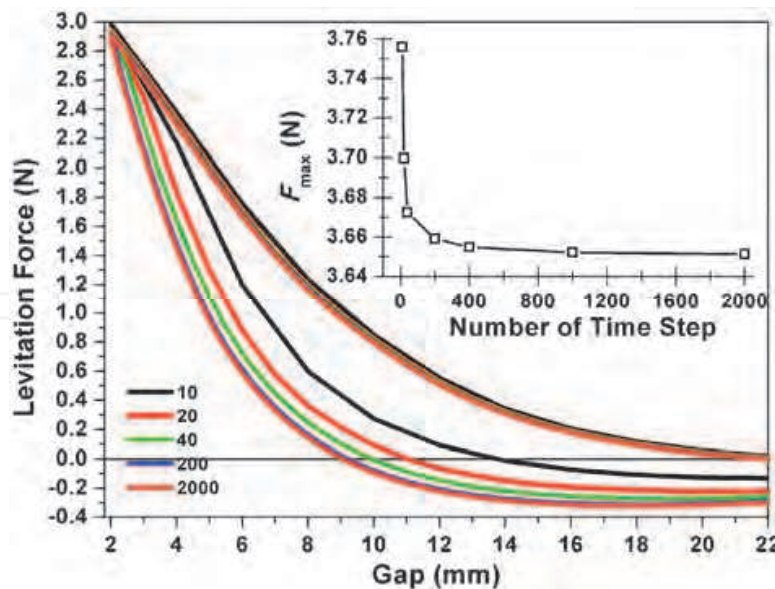
Fig. 3. Levitation force versus gap with different number of time step and the maximum levitation force F_{max} as a function of the number of time step (inset).

reduced, e.g., the rate of the increment is about 57.1% when the total finite element node is raised from 27 to 64, but it is only 2.1% when the node is raised from 343 to 512. This indicates that the computed result is consistent with the finite-element thoery, i.e., the computed value will approach to the real value with the continuous increment of mesh density. Fig. 3 plots the levitation force versus gap curve with different number of time steps and the dependence of the F_{max} on the number of time step. It is obvious that the levitation force and its hysteresis behavior will also approach to a saturated state with the increment of the number of time step, e.g., the reduced rate of the F_{max} is less than 0.024% when the number of time step is raised from 1000 to 2000 and the value of the two cases is almost identical as shown in the inset of Fig. 3. This indicates that, the approach used to handle the coupling problem of the governing equations is applicable when the number of time step adopted is sufficiently large.

4. Experimental validation

The experimental validation is of great importance to support the development of any theoretical model and to confirm the practical application of the theoretical mode to the real world. Compared with the previous validations of the model, we will validate the 3-D finite-element model in a more comprehensive way, i.e., in which two different types of motion are considered, i.e., vertical movement (perpendicular to the surface of the magnetic rail) and transverse movement (parallel to the surface of the magnetic rail), are considered, and the associated magnetic force computed with our model are compared with the experimental data.

w_{SC} (mm)	l_{SC} (mm)	t_{SC} (mm)	J_c^{ab} (A/m²)	E_c (V/m)	U_0 (eV)	ρ_f (Ωm)	a
30	30	15	$1.6×10^8$	$1×10^{-4}$	0.1	$5×10^{-10}$	3

Table 3. Parameters of the high-Tc superconductor used in the calculation for verifying the 3-D finite-element model.

3-D Finite-Element Modelling of a Maglev System
using Bulk High-Tc Superconductor and its Application
131

4.1 Brief introduction of the experiment

The self-developed maglev measurement system was used to measure the magnetic force of the bulk high-Tc superconductor (Wang, 2010). The Y-Ba-Cu-O sample used here is of single-domain with a rectangular shape, and its geometrical parameters and photo as well as its schematic drawing are presented in Table 3 and Fig. 4 respectively. The geometric parameters and photos of the two magnetic rail demonstrators (Rail_1 and Rail_2) used to generate the applied field for high-Tc superconductor are also shown in Fig. 4.

In the experiment, the sample was firstly bath-cooled in a liquid nitrogen vessel for several minutes to to insure the superconductive state was established at a certain position above the center of the magnetic rail, and then, for the vertical movement, the sample was put downward to an expected nearest gap (distance from the bottom of the high-Tc superconductor to the upper surface of the magnetic rail) and then upward to its original position in the levitation case, whereas in the suspension case, the movement was opposite; For the transverse movement, the sample was put downward (levitation case) or upward (suspension case) to its levitation height, and then it was forced to move along the transverse direction parallel to the surface of the magnetic rail (y-axis shown in Fig. 1) after a 30 seconds' relaxation at the levitation height to reduce the influence of the force relaxation on the subsequent measurement or calculation. The experimental and computed speed was chosen to be 1 mm/s in all cases and the maximum lateral displacement for traverse movement was 5 mm.
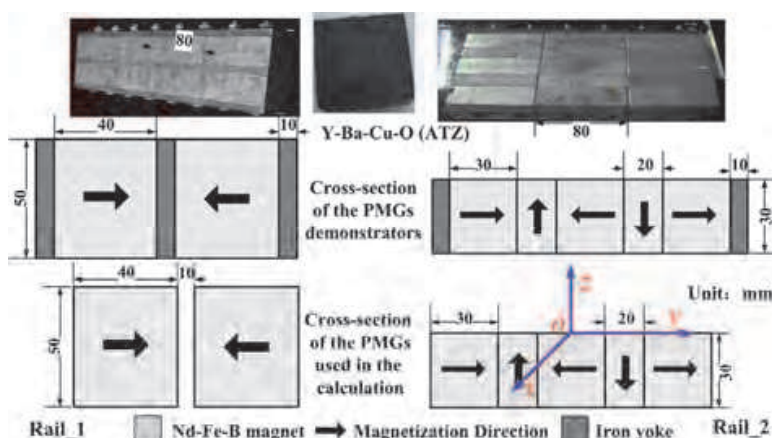
Fig. 4. Photos of the Y-Ba-Cu-O sample and magnetic rail demonstrators and associated schematic drawings of magnetic rail's cross sections.

4.2 Experimental validation of the computed results

In the calculation, the magnetic rail were calculated by a 3-D analytical model in which the finite geometry of each magnet used in the magnetic rail is taken into account (Ma, et al., 2009). With the restriction of the available experimental tools, the material parameters involved in the E–J relation and the angular-dependence of the critical current density formulation can not be directly measured. In the following calculation, the necessary material parameters were determined according to the published literatures. The reported values of the pinning potential U_0 and flow resistivity ρ_f are very scattered. Here, pinning potential and flow resistivity were chosen to be 0.1 eV and 5×10^{-10} Ωm respectively. Both of them are the frequently used values in the calculation Gou, et al.,2007a; Gou, et al.,2007b; Yoshida, et al., 1994). The anisotropic ratio for the melt-processed-single-domain Y-Ba-Cu-O has been measured to be $\sim$3 at 77 K (Murakami, et al., 1991). Critical current density in the

ab-plane J_c^{ab}, was determined by fitting one of the levitation force versus gap curve (the first curve in the following Fig. 7). In addition, Kim's model (Kim, et al., 1962) was also employed to describe the field amplitude dependence characteristic of the critical current density in the calculation. All the parameters of the Y-Ba-Cu-O were summarized in Table 3.

4.2.1 Numerical results with different E-J constitutive relations and angular-dependence of critical current density formulas

Firstly, we evaluated the levitation force versus gap behavior with different angular-dependence of the critical current density formulations and *E–J* constitutive relations. In the 3-D finite-element model, the three different components of the magnetic force, i.e., vertical force perpendicular to the surface of the magnetic rail (*z*-axis), transverse force along the magnetic rail's width (*y*-axis) and longitudinal force along the magnetic rail's length (*x*-axis) can be calculated. From the computed results presented in Fig. 5, we can see that, there is no noticeable discrepancy among the computed levitation force for different test cases. This indicates that there is almost no difference between the power law model and flux flow and creep model when the pining potential U_0 and operating temperature are identical (the index *n* in power law model is ∼ 15 at liquid nitrogen temperature with the pinning potential presented in Table 3). Moreover, the elliptical model is also viable to describe the anisotropic behavior of the high-Tc superconductor. Furthermore, as expected, the transverse force and longitudinal force shown in the inset of Fig. 5 are almost zero all the time with the variation of the gap because the applied field is symmetrical along the longitudinal and transverse directions of the magnetic rail.

In the following calculation, we choose the elliptical model for the purpose of introducing a new way to describe the anisotropic behavior of the critical current density and power law model to describe the *E–J* constitutive relation of the high-Tc superconductor because it seems to be more numerically stable to converge when compared to the flux flow and creep model.
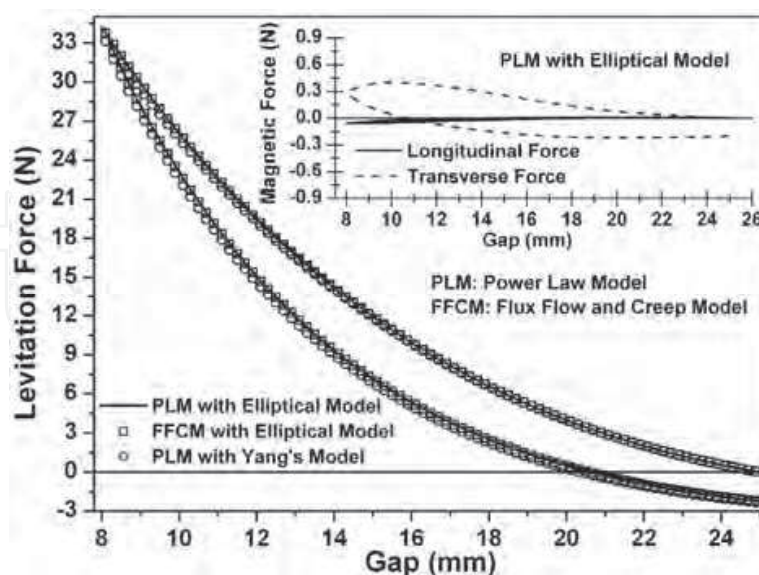

Fig. 5. Comparison of levitation force versus gap curve between different *E–J* constitutive relations and angular-dependent of the critical current density formulations as well as the transverse and longitudinal force versus gap behavior with power law and elliptical model (inset). The applied field was provided by Rail_1 shown in Fig. 4.
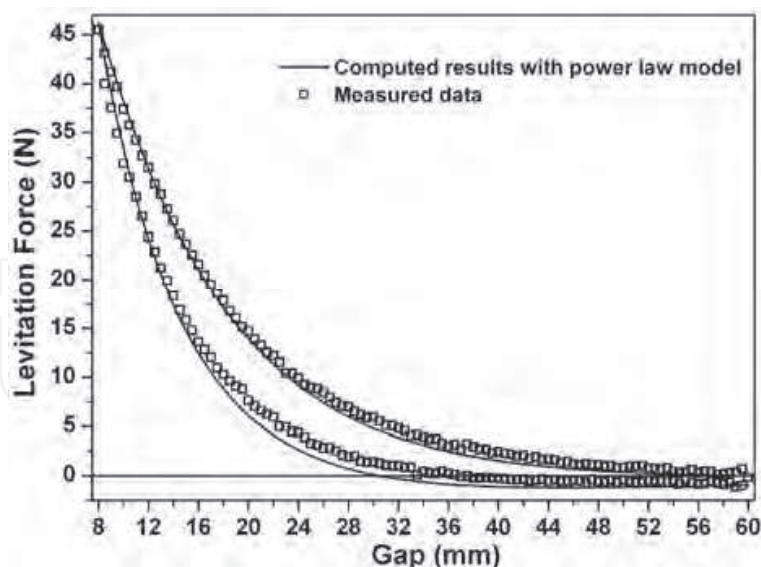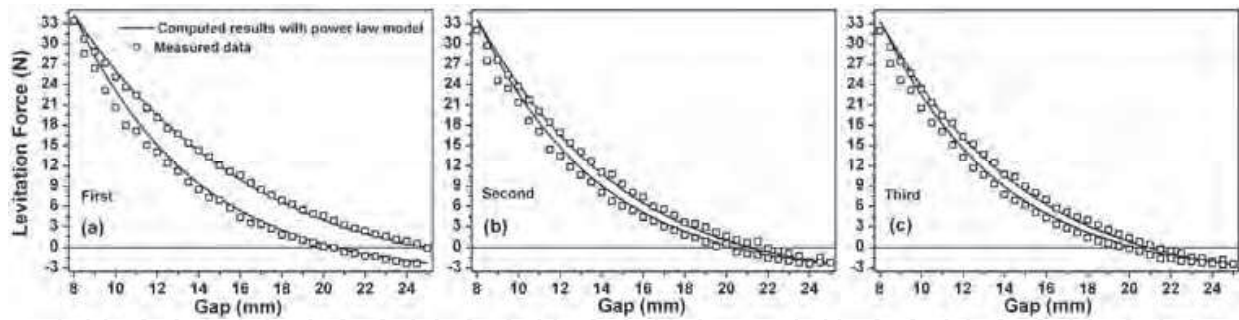
Fig. 6. Comparison of the levitation force versus gap curve between the computed results and measured results under vertical movement in the applied field generated by Rail_1 shown in Fig. 4. The Y-Ba-Cu-O was bath-cooled at a position which was 60 mm above the rail where the applied field is weak and so this case can be approximately considered as zero field-cooled condition.

4.2.2 Comparison of the levitation force under vertical movement

The vertical force of the Y-Ba-Cu-O above the center of the magnetic rail1 with different field-cooled positions was calculated and compared with the measured data. From the compared results presented in Figs. 6-8, we can see that, the computed results agree well with the measured results in both hysteresis loop as well as detailed values at a certain gap.

For the levitation case shown in Figs. 6-7, we can find from both the computed and measured results that, on the downward branch of the levitation force versus gap curve, the levitation force and slope of the curve are continuously enhanced with the decrease of the gap. For the same gap, the levitation force of the downward branch is always larger than that of the upward branch, and this reveals an obvious hysteresis behavior of the levitation force. Furthermore, the levitation force versus gap behavior was calculated and measured another two times after the first one for the field-cooled test case at 25 mm above the magnetic rail1. It can be seen clearly that the computed results also compare well with the measured data for the second time and third time. This further confirms the validation of the 3-D finite-element method.

For the suspension test case shown in Fig. 8, the suspension force versus gap curve of both computed and measured cases indicates that, according to the stiffness defined in (Hull, 2000), the suspension force increases with the gap and its stiffness is always positive before the maximum absolute value of the suspension force is achieved at a certain gap. Therefore, the suspension system is always stable within this gap. The suspension force will decrease when the gap is further increased and the suspension system becomes unstable. Also, there is a clear hysteresis behavior of the suspension force by comparing the upward and downward branch of the curve. In addition, we also presented the computed results with flux flow and creep model, and the good agreement between the results of power law model and flux flow and creep model demonstrates that, the two E–J constitutive relations are also identical for the suspension case.

Fig. 7. Comparison of the levitation force versus gap curve between the computed results and measured results under vertical movement in the applied field generated by Rail_1 shown in Fig. 4. The Y-Ba-Cu-O was bath-cooled at a position of 25 mm above the rail which was a typical field-cooled condition. The levitation force versus gap curve was calculated and measured with continous three times here.
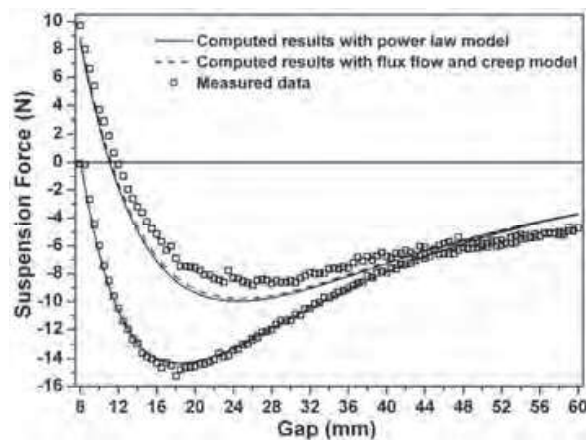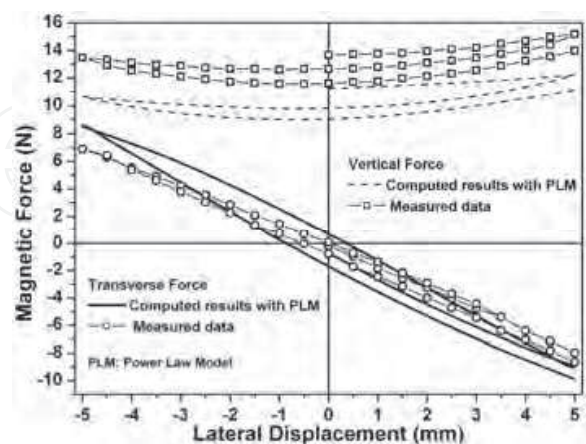

Fig. 8. Comparison of the suspension force versus gap curve between the computed results and measured results under vertical movement in the applied field generated by Rail_1 shown in Fig. 4. The Y-Ba-Cu-O is bath-cooled at a position of 8 mm above the rail.
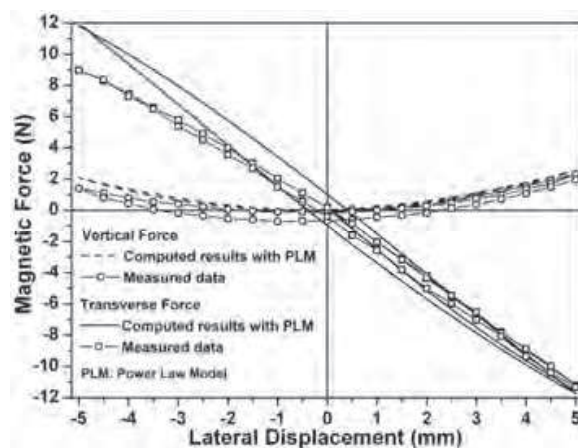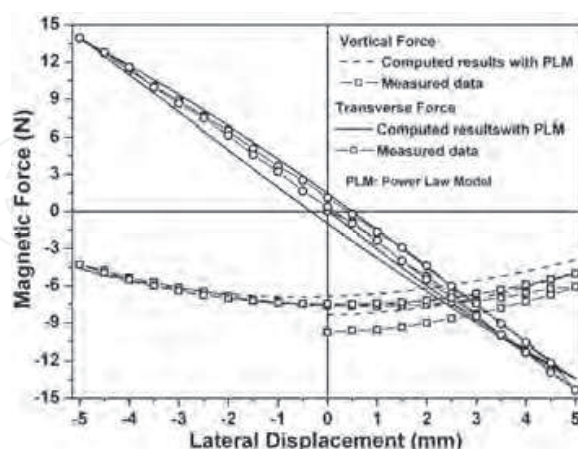

Fig. 9. Comparison of the magnetic force as a function of lateral displacement between the computed and measured results under transverse movement in the applied field generated by Rail_2 shown in Fig. 4. The Y-Ba-Cu-O sample was field-cooled at a position of 30 mm, and the levitation gap where the magnetic force was calculated or measured was 18 mm above the rail.

4.2.3 Comparisons of the magnetic force under transverse movement

In order to verify the robustness of the performance of the 3-D finite-element model, the Rail_2 shown in Fig. 4, which is a Halbach array (Halbach, 1985), was employed to produce the applied field in this section.

During the transverse movement, both the vertical force and transverse force are a function of the lateral displacement. The compared results between the numerical results and measured results for different cases, i.e., levitation case with field-cooled above the levitation position, field-cooled at the levitation position, and suspension case with field-cooled below the suspension position, are presented in Figs. 9-11, respectively.

Both the numerical results and measured results shown in Figs. 9-11 indicate that, the absolute value of the transverse force increases with the lateral displacement and the

Fig. 10. Comparison of the magnetic force as a function of lateral displacement between the computed and measured results under transverse movement in the applied field generated by Rail_2 shown in Fig. 4. The Y-Ba-Cu-O sample was field-cooled at the identical height (18 mm) with the levitation height where the magnetic force was calculated or measured.

Fig. 11. Comparison of the magnetic force as a function of lateral displacement between the computed and measured results under transverse movement in the applied field generated by Rail_2 shown in Fig. 4. The Y-Ba-Cu-O sample is field-cooled at a position of 13 mm, which was below the levitation gap (18 mm) where the magnetic force was calculated or measured.

direction of the transverse force is opposite to the transverse movement, which indicates an inheret stable levitation can be acquired. Also, the magnetic force (i.e., the vertical force and the transverse force) are hysteretic as a function of the lateral displacement. Despite that the compared results of the transverse case is not as good as that of vertical case, as a whole, the numerical results are well comparable to the measured results in quality especially for the suspension case shown in Fig. 11. The fitting value of the critical current density in the *ab*-plane J_c^{ab} was derived from the case above the Rail_1 and the shift of the applied field are likely to be responsible for the discrepancy between the computed and measured results.

5. Optimization of the magnetic rail using the 3-D finite-element model

Magnetic rail is a key component to privide the applied magnetic field for the present magnet levitation system using bulk high-Tc superconductor, and the cost spend in building the magnetic rail occupies most part of the entire investment because the magnetic rail is required along the whole line. It is thereby meaningful to optimize the structure and geometric parameters of the magnetic rail in the purpose of getting a magnetic rail that holds the required levitation capability with a reduced cost. In this aspect, a lot of previous work has been reported and the dependence of the levitation force/guidance force on the parametes of the magnetic rail has been invesigated. However, all of these results were concluded from the numerical data calculated by a 2-D model that can just fit the experimental results in quality but fails in quantity with a reasonable value of critical current density (Song, et al., 2006; Dias, et al., 2010).

w_{SC} (mm)	l_{SC} (mm)	t_{SC} (mm)	J_c^{ab} (A/m²)	E_c (V/m)	U_0 (eV)	a
42	21	9	2.5×10^8	1×10^{-4}	0.1	3

Table 4. Parameters of high-Tc superconductor used in the calculation for obtaining an optimized magnetic rail.
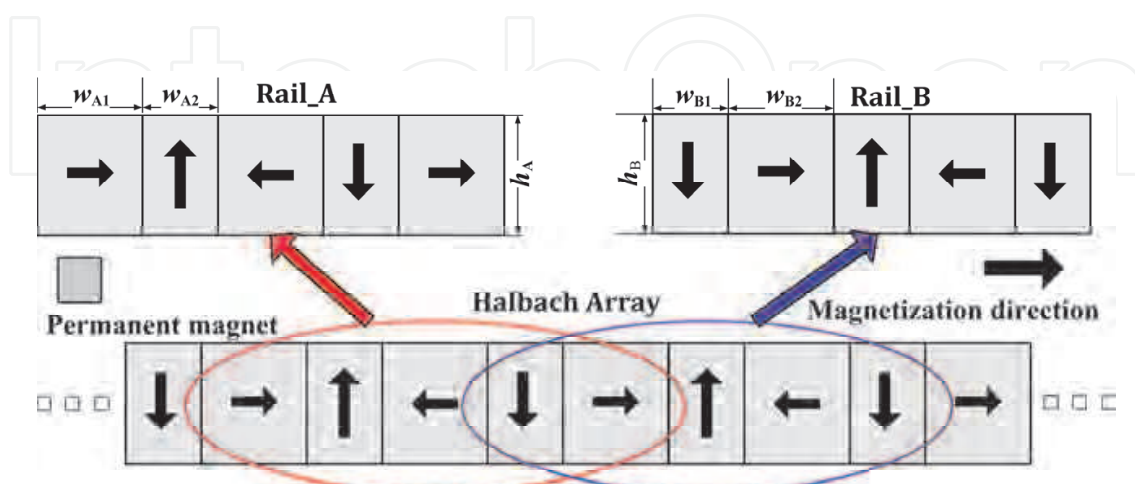

Fig. 12. Two different magnetic rails with five permanent magnets derived from the Halbach array
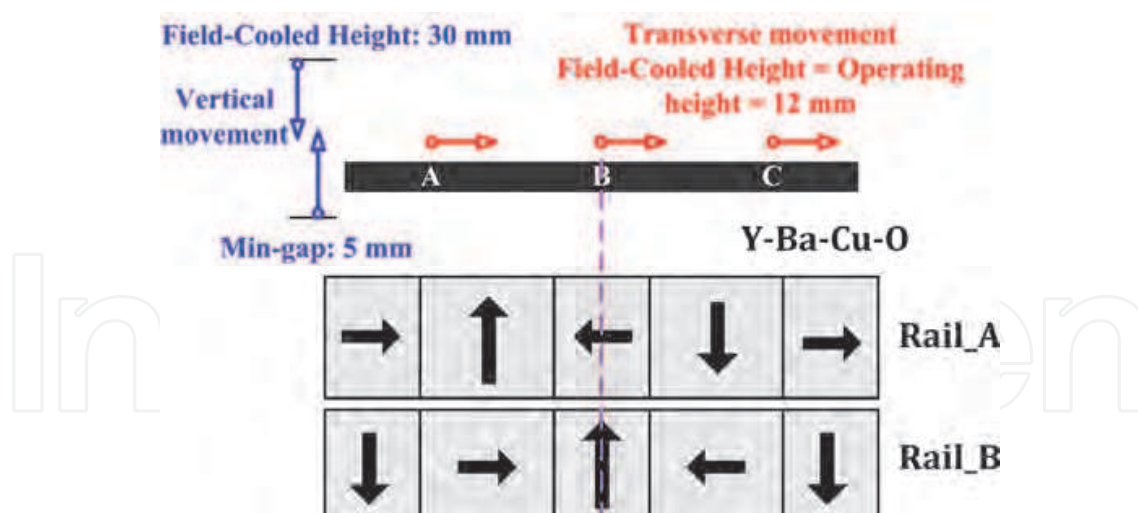
Fig. 13. Chart of the the maglev system with three bulk Y-Ba-Cu-O undergoing the vertical or transverse movement above the rail

In this section, basing on the 3-D finite-element model introduced in this chapter, we calculate the levitation force and guidance force of three Y-Ba-Cu-O bulks samples above two differnt magnetic rails deriving from the traditional Halbach array. The geometric parameters of magnetic rail such as height, width are variable in the calculation, and then the depedence of levitation capability of the bulk Y-Ba-Cu-O on those parameters was studied. Compared with the previous work, the merit of the present calculation is that, the computed levitation force/guidance force is comparable to the real system with reasonable vaule of the critical current density and thus, the computed results can be used to conduct the practical design directly.

The geometric and material parameters of the Y-Ba-Cu-O sample were shown in Table 4 The speed of the samples in both vertical and transverse direction is 1 mm/s and the magnetization M_0 of the permanent magnet employed to assemble the magnetic rail is 8.9×10^5 A/m in all cases.

As for the structure of the magnetic rail, Halbach array is a better choice than the original type used in the high-Tc superconducting maglev train demonstrator because this structure can concentrate the magnetic field to its upper space where the high-Tc superconductors are placed, and thus can improve the utilization of the magnetic field (Jing, 2007). From the basic structure of the Halbach array shown in Fig. 12, we can derive two different types of magnetic rail, i.e., one has three permanent magnets magnetized in the horizontal direction and two permanent magnets magnetized in the vertical direction, the other has three permanent magnets magnetized in the vertical direction and two permanent magnets magnetized in the horizontal direction. These two magnetic rails derived from the Halbach array are presented in Fig. 12.

In the calculation, we ignore the possible interaction among the Y-Ba-Cu-O samples for simplicity, and calculate only two samples beacuse of the symmetry of the levitation system shown in Fig. 13. In the default case, the high-Tc superconductors were field-cooled at a position of 30 mm above the surface of the magnetic rail for the calculation of the levitation force, and for the calculation of the guidance force, the tranverse movement occurs at the same height as the field-cooled position, that was 12 mm above the surface of the magnetic rail. The main parameters that should be optimized in the two structure, i.e., Rail_A and

Rail_B shown in Fig. 12, are the ratio between the width of two different magnetized magnets, the width of and the height of the magnetic rail. The following section shows the computed results of the optimization by varying those parameters.

5.1 Width ratio of the two different magnetized magnets

In this section, the levitation force and guidance force on the high-Tc superconductors with the variation of the width ratio, i.e., w_{A1}/w_{A2} for Rail_A or w_{B1}/w_{B2} for Rail_B, were calculated. In this calculation, the total width and the height of both rails were assumed respectively to be 130 mm and 30 mm and invariant with the change of the width ratio. For simplicity in drawing the following figures, the width ratio was replaced by an order and the corresponding relationship between the width ratio and the order was given in Table. 5.

Order	1	2	3	4	5	6	7	8	9	10	11
	12	13	14	15	16	17	18	19	20	21	
Width ratio	0	0.01	0.1	0.16667	0.25	0.333333	0.4	0.5	0.66667	0.83	1
	1.22	1.5	2	2.5	3	4	6	10	100	∞	

Table 5. Corresponding relationship between the width ratio and the order in optimazing the width ratio of the magnetic rails.

For the case of vertical movement, twenty-one different width ratios from zero to infinity were considered and the changing curve of the levitation force along with the width ratio at position of 5, 10, 15 and 20 mm above the Rail_A and the Rail_B was shown respectively in Fig. 14(a) and Fig. 14(b). Note that the extreme case with a width ratio of zero or infinity denotes that Halbach struture disappears and permanent magnets employed in the Rail only have one magnitized direction (vertical or horizontal direction). Both Fig. 14(a) and Fig. 14(b) display that, the levitation force, at all positions we presented, increases with the growth of the width ratio and reaches to a maximum value when the width ratio was ~0.83 for Rail_A and was ~1 for Rail_B and then drops with continuous growth of the width ratio. This finding indicates, the halbach array has a better performance because the levitation
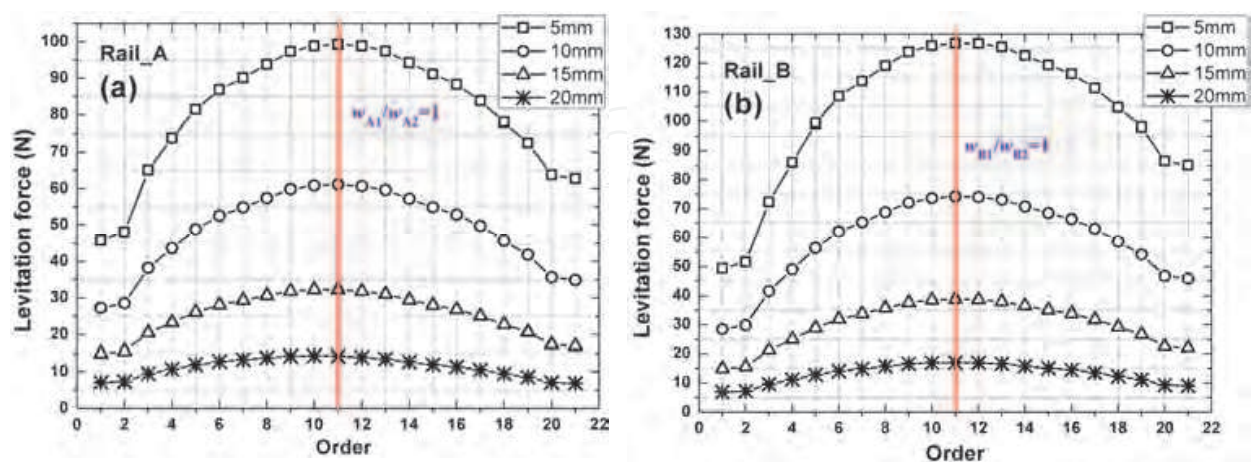

Fig. 14. The changing curve of the levitation force on the high-Tc superconductors at position of 5, 10, 15 and 20 mm above the Rail_A (a) and Rail_B (b) with the growth of the width ratio. The width ratio is replaced by an order and the corresponding relationship between the width ratio and the order (abscissa) is given in Table. 5.
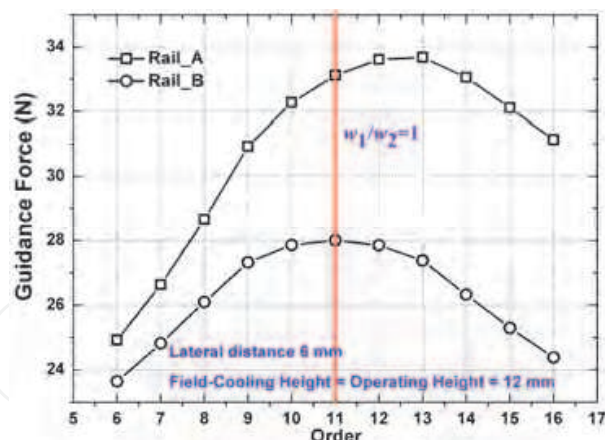
Fig. 15. The changing curve of the guidance force on high-Tc superconductors at a lateral displacement of 6 mm with the growth of the width ratio. The corresponding relationship between the width ratio and the order (abscissa) can be found in Table. 5. The total number of width ratio considered in this calculation was reduced and thus the order starts at 6 and ends at 16 .

force at the extreme case is always the smallest one as has been verified by experiment (Jing, et al., 2007; Sotelo, et al., 2010), on the other hand, the optimized struture for Rail_A is that the width of magnet magnetized in horizontal direction is slightly larger than that magnetized in vertical direction, but for Rail_B, the two type magnets have an identical width ratio.

For the case of the transverse movement, only eleven different width ratios around 1 were considered because larger levitation force can be obtained in that area according to the above computed results of levitation force. The high-Tc superconductors have a field-cooled height of 12 mm and then were drived transversely at the same height with a maximum lateral displacement of 6 mm. Fig. 15 presents the guidance force with respect to the width ratio for the Rail_A and the Rail_B. We can find from this figure that, the guidance force exhibits a same tendency with the growth of the width ratio as that found in the case of levitation force, but the width ratio where the largest guidance force occurs is found to be 1.22~1.5 for Rail_A and is still ~1 for Rail_B.

As a whole, we suggest that, for the Halbach array as the magnetic rail used in the maglev train, the optimized width ratio between the vertical and transverse magnetized magnet is ~1.

5.2 Total width of the magnetic rail

In this calculation, the total width of both rails was a variable parameter with a fixed height of 30 mm and a fixed width ratio of 1.

Fig. 16 shows the changing curve of the levitation force on the high-Tc superconductors at positions of 5, 10, 15 and 20 mm above the Rail_A and Rail_B with the growth of the total width from 60 mm to 170 mm. These figures show that, with the increase of the position, the total width where the maximum value of the levitation force appears is shift from small to large value, e.g., the levitation force increases almost linearly with the total width at the position of 20 mm for both rails and the maximum value of the levitaion force even does not appear within our calculational range. This figure also indicates that, the increase of the total width does not always bring an ehencement of the levitation force especially for the case at a
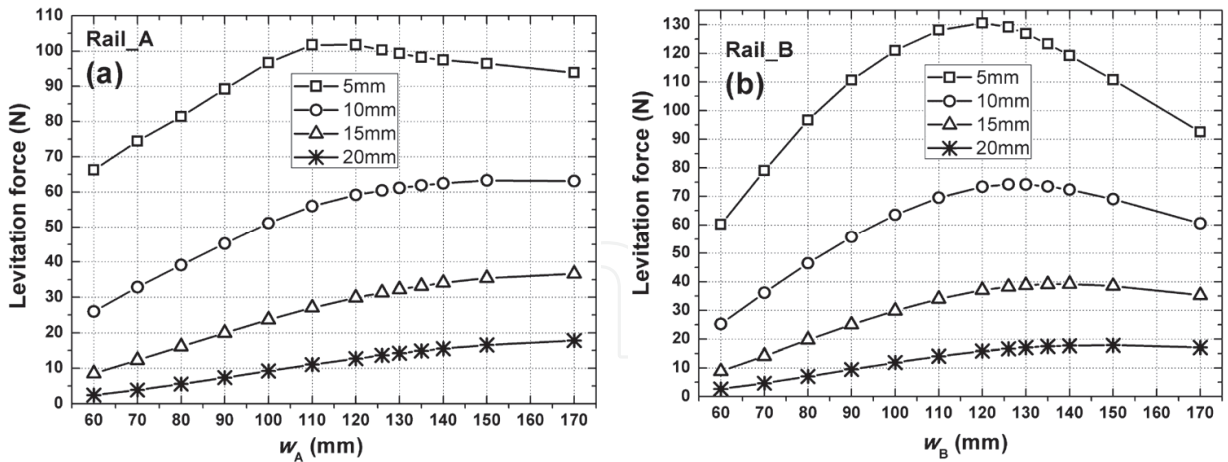
Fig. 16. The changing curve of the levitation force on the high-Tc superconductors at positions of 5, 10, 15 and 20 mm above the Rail_A (a) and Rail_B (b) with the growth of the total width. The total width was varied from 60 to 170 mm.
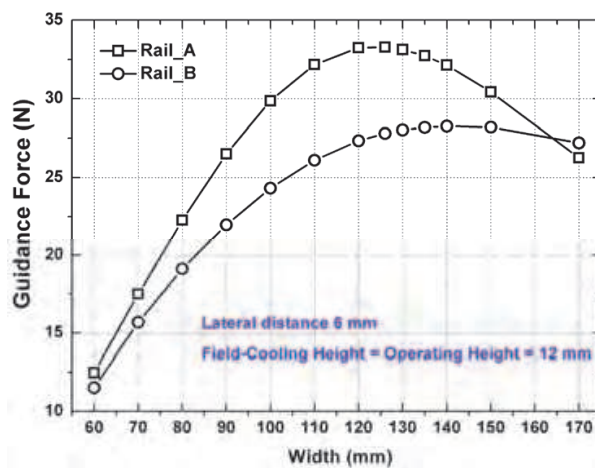

Fig. 17. The changing curve of the guidance force on the high-Tc superconductors at a lateral placement of 6 mm with the growth of the total width. The total width was varied from 60 to 170 mm.

low position. Of course, if a larger levitaion capability is required at a high position, it is a viable way to lengthen the total width of the rail. For the typical position of 15 mm in the maglev train, it seems that, the optimized value of the total width appears around 130 mm for both rails because the slope of the curve begins to dcrease at this value.

Fig. 17 shows the changing curve of the guidance force on the high-Tc superconductors at a lateral displacement of 6 mm with the growth of the total width from 60 to 170 mm. From this figure, we can find that, the guidance force also increases firstly and then decreases with the growth of the total width, and the maximum value of the guidance force occurs around 120 mm for Rail_A and around 135 mm for Rail_B. Although the total width where the maximum value of the guidance force occurs is scattered above Rail_A and Rail_B, the variation of the guidance force above both rails in the range of 120~140 mm is not evident. It is therefore this range can be considered as the optimized range which is comparable to

3-D Finite-Element Modelling of a Maglev System
using Bulk High-Tc Superconductor and its Application
141

the total width of the high-Tc superconductors (126 mm) in determining the total width of the rail for a practical design.

5.3 Height of the magnetic rail

The height of the magnetic rail is another factor influencing the levitation capability of the high-Tc superconductor. Here, we fixed the width ratio to be 1 and total width to be 130 mm, and varied the height of the magnetic rail from 15 mm to 100 mm. The levitation forces above the Rail_A and Rail_B were plotted as a function of the height and the associate curves were given in Fig. 18. This figure displays clearly that, no matter the position where the high-Tc superconductors are placed, the levitation force increases drastically at first and then goes into gradually a saturated state with heightening the rail. This phenomenon indicates that, considering the cost of the rail, it is not reasonable to get a better levitation performance by increasing the height of the rail when the height is already high enough.
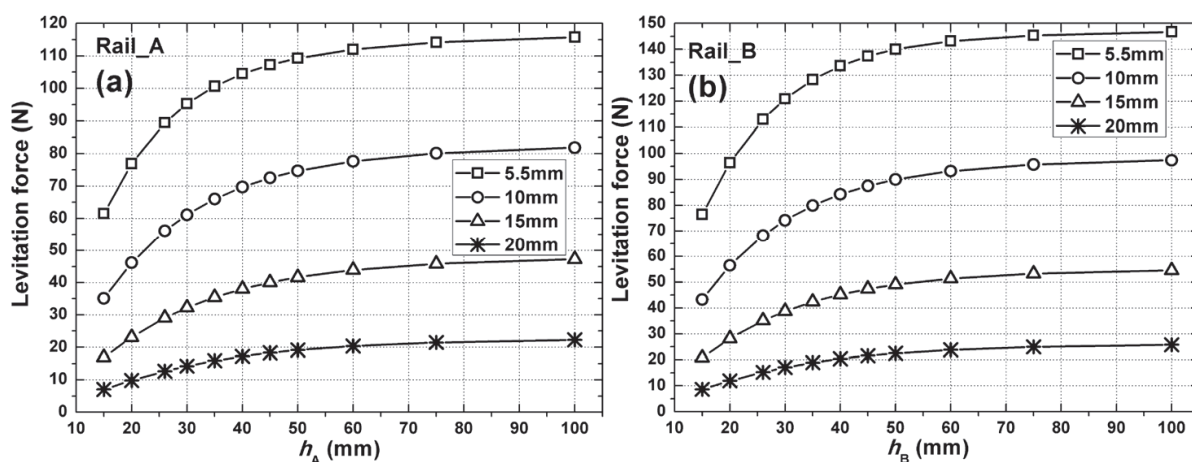

Fig. 18. The levitation force versus height of the Rail_A (a) and of the Rail_B (b). The height of both rails were varied from 15 to 100 mm.

6. Conclusion remarks

On the basis of Maxwell's equations and Helmholtz's theorem, the 3-D governing equations containing the anisotropic behavior of the HTS were deduced at length by introducing a current vector potential $\mathbf{T}$ and a simplified expression of the resistivity tensor for the high-Tc superconductor. The two common models to handle the highly nonlinear E–J characteristic, i.e., power law model and flux flow and creep model, were presented and, the critical current density J_c as a function of the angle φ between the orientation of the applied field and the c-axis of the high-Tc superconductor, was expressed by an elliptical model. The discrete matrix of the 3-D governing equations was derived by utilizing the Galerkin's finite-element method and the Crank-Nicolson-θ method to numerically treat the governing equations one by one in space and time domain respectively. The corresponding nonlinear algebraic equations of the discrete matrix were effectively resolved by incorporating the Newton-Raphson method with an extended format of the Incomplete Cholesky-Conjugate Gradientmethod.

The computed results of the levitation force of a bulk high-Tc superconductor above a magnetic rail indicate that, the levitation force and associated hysteresis behavior will

approach to a saturated state with the increment of the mesh density or the number of the time steps. This result is consistent with the finite-element theory, and also, supports the approach used to simplify the coupling problem between the differential and integral term presented in the governing equations.

Subsequentely, the 3-D finite-element model was validated by comparing the computed magnetic forces of a bulk Y-Ba-Cu-O sample with the measured data under vertical and transverse movements. Basing on the 3-D finite-element model, we also found that, the computed results of magnetic force of the high-Tc superconductor are almost identical for different angular-dependence of critical current density formulations (i.e., Yang's model and elliptical model) and $E–J$ constitutive relations (i.e., power law model and flux flow and creep model).

Lastly, using this 3-D finite-element model, we conduct a preliminary numerical work with aim of geting an optimized geometric parameter of the magnetic rails derived from the Halbach array. The results show that, when the width ratio of the two different magnetized magnets used in the magnetic rail is approximately identical and the total width of the rail is roughly indentical to the width of the high-Tc superconductors, the rail exhibits a better performance in considering both the levitation capability and the cost (be proportional to the voulme of the rail). Moreover, the levitation force has a saturated tendency with increasing continuely the height of the rail, so it is not reasonable to get a better levitation performance by increasing the height of the rail when the height is already high enough.

7. Acknowledgments

8. References

Alloui, L. & Bouillault, F. & Mimoune, S. M. (2009). Numerical study of the influence of flux creep and of thermal effect on dynamic behaviour of magnetic levitation systems with a high-Tc superconductor using control volume method. *Eur. Phys. J. Appl. Phys.*, Vol. 45, pp. 20801

Alonso, D. R. & Coombs, T. A. & Campbell, A. M. (2004). Numerical analysis of high-temperature superconductors with the critical-state model. *IEEE Trans. Appl. Supercond.*, Vol. 14, No. 4, pp. 2053–2063.

Anderson, P. W. (1962). Theory of flux creep in hard superconductor. *Phys. Rev. Lett.*, Vol. 9, No. 7, pp. 309–311

Bean, C. P. (1964). Magnetization of high-field superconductors. *Rev. Mod. Phys.*, vol. 36, pp.31–39

Brandt, E. H. (1989). Levitation in physics. *Science*, vol. 243, pp. 349–355

Brandt, E. H. (1996). Superconductors of finite thickness in a perpendicular magnetic field: Strips and slabs. *Phys. Rev. B*, Vol. 54, No. 6, pp. 4246–4264

Cui, X. (1989). A new preconditional conjugate gradient algorithm. *Journal of North China Institute of Electric Power*, No. 2, pp. 1–8, (in Chinese)

Davis, L. C. & Logothetis, E. M. & Soltis, R. E. (1988). Stability of magnets levitated above superconductors. *J. Appl. Phys.*, Vol. 64, No. 8, pp. 4212–4218

Dias, D. H. N. & Motta, E. S. & Sotelo, G. G. & Andrade Jr, R. D. (2010). Experimental validation of field cooling simulations for linear superconducting magnetic bearings. *Supercond. Sci. Technol.* Vol. 23, pp. 075013

Dinger, T. R. & Worthington, T. K. & Gallagher, W. J. & and Sandstrom, R. L. (1987). Direct observation of electronic anisotropy in single-crystal $Y_1Ba_2Cu_3O_{7-x}$. *Phys. Rev. Lett.*, Vol. 58, pp. 2687–2690

Fujiwara, K. & Nakata, T. & Fusayasu, H. (1993). Acceleration of convergence characteristic of the ICCG method. *IEEE Trans. Magn.*, Vol. 29, No. 2, pp. 1958–1961

Gou, X. F. & Zheng, X. J. & Zhou, Y. H. (2007a). Drift of levitated/suspended Body in high-T_c superconducting levitation systems under vibration—part I: A criterion based on magnetic force-gap relation for gap varying with time. *IEEE Trans. Appl. Supercond.*, Vol. 17, No. 3, pp. 3795–3802

Gou, X. F. & Zheng, X. J. & Zhou, Y. H. (2007b). Drift of levitated/suspended Body in high-T_c superconducting levitation systems under vibration—Part II: drift velocity for gap varying with time. *IEEE Trans. Appl. Supercond.*, Vol. 17, No. 3, pp. 3803–3808

Grilli, F. & Stavrev, S. & Le Floch, Y. & Costa-Bouzo, M. & Vinot, E. & Klutsch, I. & Meunier, G. & Tixador, P. & Dutoit, B. (2005). Finite-element method modeling of superconductors: from 2-D to 3-D. *IEEE Trans. Appl. Supercond.*, Vol. 15, No. 1, pp. 17–25

Halbach, K. (1985). Application of permanent magnets in accelerators and electron storage rings (invited). *J. Appl. Phys.*, Vol. 57, pp. 3605–3908

Hashizume, H. & Sugiura, T. & Miya, K. & Ando, Y. & Akita, S. & Torii, S. & Kubota, Y. & T. Ogasawara. (1991). Numerical analysis of a. c. losses in superconductors. *Cryogenics*, Vol. 31, pp. 601–606

Hull, J. R. & Cansiz, A. (1999). Vertical and lateral forces between a permanent magnet and a high-temperature superconductor. *J. Appl. Phys.*, Vol. 86, No. 11, pp. 6396–6404

Hull, J. R. (2000). Superconducting bearings. *Supercond. Sci. Technol.*, vol. 13, pp. R1–R15

Jing, H. & Wang, J. & Wang, S. & Wang, L. & Liu, L. & Zheng, J. & Deng, Z. & Ma, G. & Zhang, Y. & Li. J. (2007). A two–pole Halbach permanent magnet guideway for high temperature superconducting Maglev vehicle. *Physica C*. 2007, Vol. 463–465, pp. 426–430

Kershaw, D. S. (1978). The incomplete cholesky–conjugate gradient method for the iterative solution of systems of linear equations. *Journal of Computational Physics*, Vol. 26, pp. 43–65

Kim, Y. B. & Hemptead, C. F. & Strnad, A. R. (1962). Critical persistent currents in hard superconductors. *Phys. Rev. Lett.*, Vol. 9, No. 7, pp. 306-309

Kordyuk, A. A. (1998). Magnetic levitation for hard superconductor. *J. Appl. Phys.*, Vol. 83, No. 1, pp. 610–612

Krusin-Elbaum, L. & Malozemoff, A. P. & Yeshurun, Y. & Cronemeyer, D. C. & Holtzberg, F. (1989). Temperature dependence of lower critical fields in Y-Ba-Cu-O crystals. *Phys. Rev. B*, Vol. 39, No. 4, pp. 2936–2939

Lu, Y. Y. & Wang, J. S. & Wang, S. Y. & Zheng J., (2008). 3D-Modeling numerical solutions of electromagnetic behavior of HIGH-TC SUPERCONDUCTORC bulk above permanent magnetic guideway. *J. Supercond. Nov. Magn.*, Vol. 21, pp. 467–472

Luo, Y. & Takagi, T. & Miya, K. (1999). Reduction of levitation decay in high Tc superconducting magnetic bearings. *Cryogenics*, Vol. 39, pp. 331–338

Ma, G. T. & Liu, H. F. & Wang, J. S. & Wang, S. Y. & Li, X. C. (2009). 3D modeling permanent magnet guideway for high temperature superconducting maglev vehicle application. *J. Supercond. Nov. Magn.*, Vol. 22, pp. 841–847

Ma, K. B. & Postrekhin, Y. V. & Chu, W. K. (2003). Superconductor and magnet levitation devices. *Rev. Sci. Instrum.*, Vol. 74, No. 12, pp. 4989–5017

Matsushita, T. (2007). *Flux Pinning in Superconductors.* Springer-Verlag Berlin, pp. 365-366.

Mikitik, G. P. & Brandt, E. H. (2000). Critical state in thin anisotropic superconductors of arbitrary shape. *Phys. Rev. B*, Vol.62, pp. 6800–6811

Miya, K. & Hashizume, H. (1988). Application of T-method to A.C. problem based on boundary element method. *IEEE Trans. Magn.*, Vol. 24, No. 1, pp. 134–137

Murakami, M. & Oyama, T. & Fujimoto, H. & Gotoh, S. & Yamaguchi, K. (1991). Melt processing of bulk high Tc superconductors and their application. *IEEE Trans. Magn.*, Vol. 27, No. 2, pp. 1479–1486

Napoli, A. D. & Paggi, R. (1983). A model of anisotropic grain-oriented steel. *IEEE Trans. Magn.*, Vol. 19, No. 4, pp. 1557–1561

Navau, C. & Sanchez, A. (2001). Magnetic properties of finite superconducting cylinders. II. Nonuniform applied field and levitation force. *Phys. Rev. B*, Vol. 64, pp. 214507

Pecher, R. & McCulloch, M. D. & Chapman, S. J. & Prigozhin, L. & Elliot, C. M. (2003) 3D-Modelling of bulk type-II superconductors using unconstrained H-formulation. *EUCAS 2003*, Sorrento, Italy, Sep. 14–18

Prigozhin, L. (1997). Analysis of Critical-State Problems in Type-II Superconductivity," *IEEE Trans. Appl. Supercond.*, Vol. 7, No. 4, pp. 3866–3873

Qin, M. J. & Li, G. & Liu, H. K. & Dou, S. X. & Brandt, E. H. (2002). Calculation of the hysteretic force between a superconductor and a magnet. *Phys. Rev. B*, Vol. 66, pp. 024516

Rhyner, J. (1993). Magnetic properties and AC–losses of superconductors with power law current–voltage characteristics. *Physica C*, Vol. 212, pp. 292–300

Sanchez, A. & Navau, C. (2001). Magnetic properties of finite superconducting cylinders. I. Uniform applied field. *Phys. Rev. B*, Vol. 64, pp. 214506

Sanchez, A. & Valle, N. D. & Pardo, E. & Chen, D. X. & Navau, C. (2006). Magnetic levitation of superconducting bars. *J. Appl. Phys.*, Vol. 99, pp.113904

Sawamura, M. & Tsuchimoto, M. (2000). Numerical analysis for superconductor in sheet and bulk form," *Japan J. Indust. Appl. Math.*, Vol. 17, No. 2, pp. 199–208

Schultz, L. & Haas, O. & Verges, P. & Beyer, C. & Röhlig, S. & Olsen, H. & Kühn, L. & Berger, D. & Noteboom, U. & Funk, U. (2005). Superconductively levitated transport system-the SupraTrans project. *IEEE Trans Appl. Supercond.*, Vol. 15, No.2, pp. 2301–2305

Song, H. H. & Wang, J. S. & Wang, S. Y. & Ren, Z. Y. & Wang, X. R. & Haas, O. & Fuchs, G. & Schultz, L. (2006). Studies of YBCO electromagnetic properties for high-temperature superconductor maglev technology. in *New Topics in Superconductivity Research*, Barry P. Martins Ed., New York: Nova Science Publishers, pp. 107–156

Sotelo, G. G. & Dias, D. H. N. & Andrade Jr, R. D. & Stephan, R. M. (2010). Tests on a Superconductor Linear Magnetic Bearing of a Full-Scale MagLev Vehicle. *IEEE Trans. Appl. Supercond.*, doi: 10.1109/TASC.2010.2086034, (in press)

Takagi, T. & Sugiura, T. & Miyata, K. & Norimatsu, S. & Okamura, K. & Miya, K. (1988). Iterative solution technique for 3-D eddy current analysis using T-method. *IEEE Trans. Magn.*, Vol. 24, No. 6, pp. 2682–2684

Ueda, H. & Azumaya, S. & Tsuchiya, S. & Ishiyama, A. (2006). 3D electromagnetic analysis of levitating transporter using bulk superconductor. *IEEE Trans. Appl. Supercond.*, Vol. 16, No. 2, pp. 1092–1095

Uesaka, M. & Yoshida, Y. & Takeda, N. & Miya, K. (1993). Experimental and numerical analysis of three-dimensional high-T_c superconducting levitation systems. *Int. J. Appl. Electromagn. Mater.*, Vol. 4, pp. 13–25

Wang, J. S. & Wang, S. Y. & Zeng, Y. W. & Huang, H. Y. & Luo, F. & Xu, Z. P. & Tang, Q. X. & Lin, G. B. & Zhang, C. F. & Ren, Z. Y. & Zhao, G. M. & Zhu, D. G. & Wang, S. H. & Jiang, H. & Zhu, M. & Deng, C. Y. & Hu, P. F. & Li, C. Y. & Liu, F. & Lian, J. S. & Wang, X. R. & Wan, L. H. & Shen, X. M. & Dong, X. G. (2002). The first man-loading high temperature superconducting maglev test vehicle in the world. *Physica C*, Vol. 378-381. pp.809-814

Wang, J. S. & Wang, S. Y. (2010). *High Temperature Superconducting Maglev Measurement System*. In: Milind Kr Sharma Ed., Advances in Measurement Systems, pp. 51-80

Wu, J. Z. & Hsieh, P. Y. & McGuire, A. V. & Schmidt, D. L.& Wood, L. T. & Shen, Y. & Chu, W. K. (1991). Anisotropic properties of the high–quality epitaxial $YBa_2Cu_3O_{7-\delta}$ (110) thin film. *Phys. Rev. B*, Vol. 44, No. 22, pp. 12643–12646

Yamafuji, K. & Mawatari, Y. (1992). Electromagnetic properties of high Tc superconductors: relaxation of magnetization. *Cryogenics*, Vol. 32, No. 6, pp. 569–577

Yang, W. M. & Feng, Y. & Zhou, L. & Zhang, P. X. & Wu, M. Z. & Chen, S. K. & Wu, X. Z. & Gawalek, W. (1999). The effect of the grain alignment on the levitation force in single domain $YBa_2Cu_3O_y$ bulk superconductors. *Physica C*, Vol. 319, pp. 164–168

Yang, Y. & Zheng, X. J. (2007). Method for solution of the interaction between superconductor and permanent magnet. *J. Appl. Phys.*, Vol. 101, pp. 113922

Yoshida, Y. & Uesaka, M. & K. Miya, (1994). Magnetic field and force analysis of high-Tc superconductor with flux flow and creep. *IEEE Trans. Magn.*, Vol. 30, No. 5, pp. 3503–3506

Wang Jiasu and Wang Suyu, (2005). Synthesis of Bulk Superconductors and Their Properties on Permanent Magnet Guideway. In: Anant Narlikar Ed., Frontiers in Superconducting Materials (Springer Verlag, Germany), pp.885-912
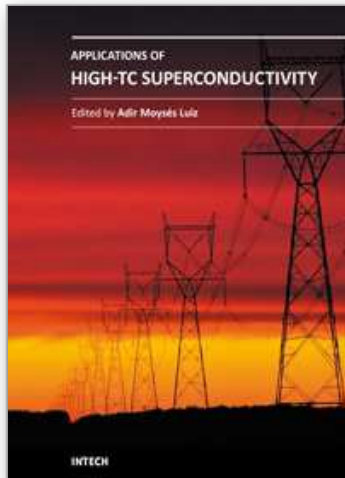
Applications of High-Tc Superconductivity

Edited by Dr. Adir Luiz

This book is a collection of the chapters intended to study only practical applications of HTS materials. You will find here a great number of research on actual applications of HTS as well as possible future applications of HTS. Depending on the strength of the applied magnetic field, applications of HTS may be divided in two groups: large scale applications (large magnetic fields) and small scale applications (small magnetic fields). 12 chapters in the book are fascinating studies about large scale applications as well as small scale applications of HTS. Some chapters are presenting interesting research on the synthesis of special materials that may be useful in practical applications of HTS. There are also research about properties of high-Tc superconductors and experimental research about HTS materials with potential applications. The future of practical applications of HTS materials is very exciting. I hope that this book will be useful in the research of new radical solutions for practical applications of HTS materials and that it will encourage further experimental research of HTS materials with potential technological applications.

How to reference

In order to correctly reference this scholarly work, feel free to copy and paste the following:

Guang-Tong Ma, Jia-Su Wang, and Su-Yu Wang (2011). 3-D Finite-Element Modelling of a Maglev System using Bulk High-Tc Superconductor and its Application, Applications of High-Tc Superconductivity, Dr. Adir Luiz (Ed.), ISBN: 978-953-307-308-8, InTech, Available from: http://www.intechopen.com/books/applications-of-high-tc-superconductivity/3-d-finite-element-modelling-of-a-maglev-system-using-bulk-high-tc-superconductor-and-its-applicatio

INTECH

open science | open minds